

JWST NIRSpec’s Cosmic Ray Experience at L2*

BERNARD J. RAUSCHER  ¹ AND D.J. FIXSEN^{1,2}

¹ *NASA Goddard Space Flight Center, Observational Cosmology Laboratory, Greenbelt, MD 20771, USA*

² *Center for Research and Exploration in Space Science and Technology, NASA/GSFC, Greenbelt, MD 20771, USA*

ABSTRACT

We characterize cosmic ray interactions in blanked-off *JWST* NIRSpec “dark” exposures. In its Sun/Earth-Moon L2 halo orbit, *JWST* encounters energetic ions that penetrate NIRSpec’s radiation shielding. The shielded cosmic ray hit rate decreased from approximately 4.3 to 2.3 ions $\text{cm}^{-2} \text{ s}^{-1}$ during the first three years of operation. A typical hit affects about 7.1 pixels necessitating mitigation during calibration and deposits around 6 keV in the $\lambda_{\text{co}} = 5.4 \mu\text{m}$ HgCdTe detector material (equivalent to ~ 5200 charges). The corresponding linear energy transfer is about 0.86 keV μm^{-1} . As we are currently near solar maximum, galactic cosmic ray flux is expected to increase as solar activity declines, leading to an anticipated rise in the NIRSpec rate from 2.3 to 4.3 ions $\text{cm}^{-2} \text{ s}^{-1}$ by early 2027 and potentially reaching ~ 6 ions $\text{cm}^{-2} \text{ s}^{-1}$ in the early 2030s. We investigate rare, large “snowball” hits and, less frequently, events with secondary showers that pose significant calibration challenges. We explore their possible origins as heavy ions, secondary particles from shielding, or inelastic scattering in the HgCdTe detector material. We discuss the implications of these findings for future missions including the Nancy Grace Roman Space Telescope.

1. INTRODUCTION

The James Webb Space Telescope (*JWST*; Gardner et al. 2023) was launched on December 25, 2021, and began scientific observations the following June. Since then, *JWST*’s science instruments have regularly collected blanked-off “dark” exposures for calibration purposes. These darks contain a wealth of information about the Near Infrared Spectrograph (NIRSpec) and its detectors’ response to space radiation. While NIRSpec’s radiation shielding blocks most low energy particles, high energy galactic cosmic rays (GCR) pass through. They leave ionization tracks behind that manifest mostly as small clusters of disturbed pixels or streaks. These cosmic ray “hits” are an important consideration in observation planning. Detecting and correcting for them is an important step in the calibration pipeline.

Corresponding author: Bernard J. Rauscher
 Bernard.J.Rauscher@nasa.gov

Dale.J.Fixsen@nasa.gov

* Published in PASP, 137, 095003 (2025); DOI: 10.1088/1538-3873/adfb2f

The purpose of this article is to describe the appearance of NIRSpec cosmic rays from the perspective of astronomers. Our focus is on parameters and disturbances that affect observation planning and scientific data integrity. However, space radiation poses other concerns from a hardware safety and operation perspective. These effects include long-term performance degradation, single event upsets, and spacecraft charging. For more information on these topics, the interested reader is referred to Barth et al. (2000) and Evans et al. (2003).

One example of performance degradation is the steady increase of inoperable “hot” pixels in the NIRSpec detectors. Since June, 2022, the rate of increase has been about 100 new hot pixels per month for each of the two detectors, or about 0.03% of all pixels per year.¹

The remainder of this paper is organized as follows. Section 2 provides more information on *JWST*. We then describe the data used in this study, including pipelined calibration and the cosmic ray finder algorithm, in Section 3. We present our results in Section 4. Section 5 compares the cosmic ray rate observed by NIRSpec with

¹ <https://jwst-docs.stsci.edu/jwst-near-infrared-spectrograph/nirspec-instrumentation/nirspec-detectors/nirspec-detector-performance#NIRSpecDetectorPerformance-Badpixels>

that of other concurrent missions. Looking ahead, Section 6 discusses our expectations for the Nancy Grace Roman Space Telescope (*Roman*). Finally, Section 7 is the summary.

2. JWST

JWST is today’s premier space observatory for 0.6 – 28 μm astrophysics. It features an approximately 6.5 m diameter cryogenic space telescope and four scientific instruments: (1) NIRSpec, (2) the Near Infrared Camera (NIRCam), (3) the Near Infrared Imager and Slitless Spectrograph (NIRISS), and (4) the Mid-Infrared Instrument (MIRI). The instruments’ detectors are exquisitely sensitive to cosmic rays in addition to light. The observatory is situated in a halo orbit around the Sun/Earth-Moon system’s second Lagrange point (L2).

Since June, 2022, NIRSpec has collected blanked-off dark exposures at regular intervals. These darks reveal the cosmic ray environment at NIRSpec’s detectors. Although the natural L2 environment provides the cosmic rays, NIRSpec’s detectors sit behind radiation shielding. The shielding blocks most low energy particles ($E \lesssim 100$ MeV). However, it is possible for low energy secondary radiation to be produced within the shielding itself. High energy GCRs easily penetrate the shielding.

We selected NIRSpec for this study because we are part of the team that built it. This provides better insight into the radiation shielding than we have for other instruments. Alone among *JWST* instruments, NIRSpec provides Improved Reference Sampling and Subtraction (IRS²; [Rauscher et al. 2017](#)). IRS² uses a specialized detector clocking pattern and reference correction software to significantly suppress correlated read noise compared to NIRCam and NIRISS. Using IRS², cosmic ray detection is less affected by detector noise than it would be for other instruments.

This section builds on two early studies of the L2 space environment that were done for *JWST*. At the time, the concept for a large, IR-optimized space telescope, was known as the Next Generation Space Telescope (NGST). Our aim here is to provide enough information about the environment for readers to understand later sections of this paper in context. For a more complete explanation of the L2 environment, we refer the interested reader to the original studies ([Barth et al. 2000](#); [Evans et al. 2003](#)).

2.1. L2 Halo Orbit and Radiation Environment

Figure 1 shows *JWST*’s orbit in relation to the Sun and the Earth-Moon gravitational system. L2 is located approximately 1.5×10^6 km from Earth on the anti-Sun

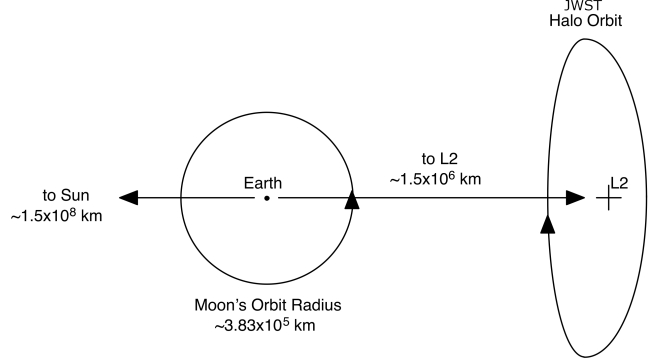


Figure 1. *JWST* is in a “halo” orbit about the Sun/Earth-Moon L2 Lagrange point. L2 is about 1.5×10^6 km from the earth, outside the Moon’s orbit, and on the opposite side of the Earth from the Sun. Credit: Based on a figure from ([Evans et al. 2003](#))

side, along the line joining the Sun and the Earth-Moon center of mass. This orbit was chosen because it allows a single sunshade to shield the observatory from the Sun, Earth, and Moon, thereby facilitating passive cooling. Moreover, *JWST*’s orbit enables observing nearly half of the sky at any given time while maintaining acceptable radio contact with Earth.

Typically, a spacecraft in a heliocentric orbit with a radius larger than Earth’s moves at a slower angular velocity, resulting in a longer orbital period and causing it to lag behind Earth. However, at the L2 point, the combined gravitational pull of the Earth and Moon provides the necessary additional acceleration for *JWST* to maintain orbital velocity commensurate with Earth’s solar orbit, thus keeping pace. The L2 halo orbit is dynamically unstable; small gravitational perturbations from other bodies tend to nudge *JWST* away from L2 into an independent solar orbit. Therefore, periodic station-keeping maneuvers are required to maintain *JWST*’s position within the halo orbit.

The Earth’s liquid outer core generates an approximately dipole magnetic field that dominates the magnetosphere within a few Earth radii. Figure 2 shows the magnetic field and plasma environment near the earth. The magnetic field deflects charged particles and thus “protects” the Earth from some radiation. However, *JWST* operates in deep space, beyond this protection.

Figure 2 shows the locations of *JWST* and two other missions that are discussed in Section 5. *JWST* is located far to the right of this figure, where the magnetosphere provides essentially no shielding. It is in deep space. *ACE* is located at L1, well to the left of this figure. It too is in deep space. The Geostationary Operational Environmental Satellites (*GOES*) are in geostationary orbits (GEO). The thick, yellow line in Figure 2

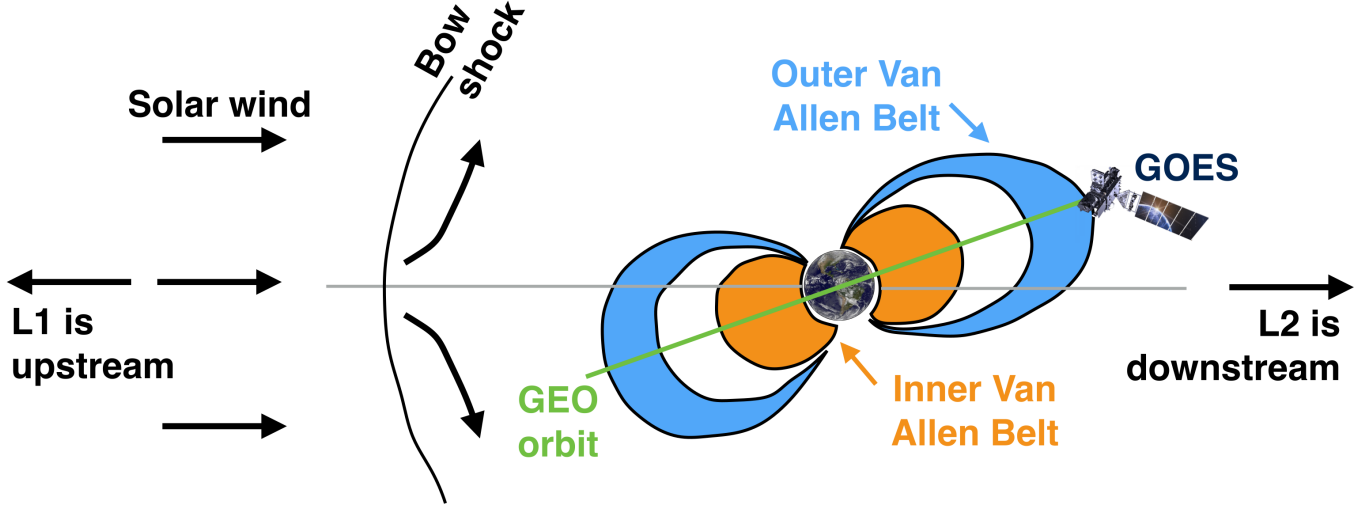


Figure 2. Noon-midnight cross section of the near-Earth environment. Magnetosphere plasma extends out to about the bow shock looking toward the sun and trails further downstream on the anti-Sun side. *JWST*'s L2 halo orbit is about $235 R_{\oplus}$ to the right of the earth. This is deep space, where the earth's magnetosphere provides essentially no shielding. The Advanced Composition Explorer (*ACE*) is located at L1. This is also deep space. We would expect *ACE* to experience a similar GCR environment to *JWST*. The *GOES* satellites are in geostationary orbits. There, the Earth's magnetic shielding provides some protection. We therefore expect *JWST* and *ACE* to see similar GCRs. One might reasonably expect *GOES* to see somewhat fewer GCRs on account of the weak, but still present protection from the earth's magnetosphere.

shows the locations of GEO orbits. The *GOES* satellites are located outside the Inner Van Allen Belt, but near the outer edge of the Outer Van Allen Belt.

The Outer Van Allen Belt is dominated by electrons that are blocked by NIRSpec's radiation shielding. Although the Earth's magnetic field is weak at GEO (~ 100 nT),² it is nevertheless significantly stronger than the $\lesssim 10$ nT Interplanetary Magnetic Field (IMF) that dominates at L2.³ Bearing these considerations in mind, we expect *ACE*'s GCR environment to be similar to *JWST*'s. We expect *GOES* to be exposed to a somewhat weaker GCR environment than *JWST* on account of the weak but still present shielding provided by the magnetosphere. Figure 2 shows several other magnetosphere features that do not concern us here. For more information, the interested reader is referred to Evans et al. (2003).

The Sun generates a solar wind of charged particles that carry a magnetic field out from the Sun. As the magnetic field spreads, it weakens until it balances the magnetic pressure of interstellar space at about 150 AU. The space within, known as the heliosphere, is domi-

nated by the solar wind and the magnetic fields that it carries.

Charged particles from the Sun are mostly low energy protons (up to ~ 50 Mev) which are shielded from the detectors by material around the detectors. GCRs from beyond the solar system are dominated ($\sim 90\%$) by few GeV protons. The remaining cosmic particles are alpha particles ($\sim 9\%$) with a few heavier elements and exotic particles. The solar magnetic field affords some protection from these particles but the solar magnetic field and thus the shielding fluctuates with the solar cycle. Cosmic radiation levels are high when solar activity and sunspots are low and vice versa.

2.2. NIRSpec

Our discussion of NIRSpec is limited to components that affect its sensitivity to cosmic rays. These are primarily the H2RG near infrared array detectors and the radiation shielding. For a full description of the instrument, the interested reader is referred to Jakobsen et al. (2022). Birkmann et al. (2022) and references therein provide more information about NIRSpec's detectors.

NIRSpec has two Teledyne H2RG HgCdTe near infrared detector arrays (Figure 3). When a photon hits the HgCdTe detector material, it typically creates an electron-hole pair. The holes are collected in pixels which charge the photodiodes' capacitances. NIRSpec's near-IR detector arrays thus convert photons into voltages in pixels. Then, the SIDECAr application specific

² See the GOES Magnetometer webpage at <https://www.swpc.noaa.gov/products/goes-magnetometer>. B_t is the magnetic field strength.

³ See the ACE real time solar wind webpage at <https://www.swpc.noaa.gov/products/ace-real-time-solar-wind> where B_t is the magnetic field strength.

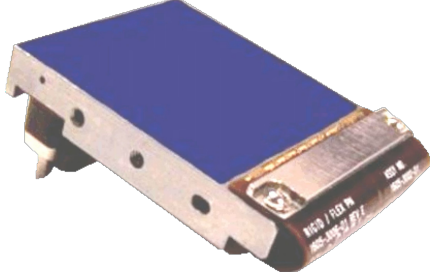


Figure 3. NIRSpec has two Teledyne H2RG HgCdTe near infrared detector arrays. Light enters from the top. Cosmic rays come in from all sides. Those that come through the bottom pass through about ≈ 7 mm of molybdenum, a thin balanced composite structure (BCS), thin layers of epoxy, a thin silicon readout integrated circuit (ROIC), and thin indium bumps before reaching the HgCdTe detector layer. The molybdenum (Mo) package is included in the shielding on the back side of the detector. The BCS is a proprietary component that Teledyne uses to minimize thermally induced strain. Everything except the molybdenum base is ignored in the shielding calculation.

integrated circuit (ASIC) readout electronics amplify and convert these voltages into digital numbers (DN) in four separate output channels for each detector.

It is standard practice in the astronomical community to parameterize near-IR array detectors in units of electrons. Although NIRSpec’s p-on-n photodiodes physically integrate holes, we nevertheless follow convention from this point forward and speak of electrons except when the difference is physically important to the discussion at hand. The conversion gains between electrons and DN, g_c (e^-/DN), were measured at NASA Goddard Space Flight Center as part of characterizing the NIRSpec Detector Subsystem (Table 1).

The pair creation energy is set by the HgCdTe bandgap energy, E_g . This is related to the cutoff wavelength by,

$$E_g = \frac{hc}{\lambda_{\text{co}}}. \quad (1)$$

Teledyne measures λ_{co} when building detectors. [Alig & Bloom \(1977\)](#) provides an empirical relation for converting the bandgap energy of a semiconductor to pair-creation energy, ϵ . It is,

$$\epsilon = 2.73E_g + 0.55 \text{ eV}. \quad (2)$$

[Fox et al. \(2009\)](#) validated this expression for HgCdTe using data from eight non-flight Hubble Space Telescope (*HST*) Wide Field Camera 3 (WFC3) Teledyne H1R arrays. Substituting Equation 1 into Equation 2 and multiplying by g_c yields the relation,

$$g_{\text{pp}} = \left(2.73 \frac{hc}{\lambda_{\text{co}} \epsilon} + 0.55 \right) g_c \quad \text{eV/DN}. \quad (3)$$

Table 1. Pair-production Gains

		λ_{co} (μm)	Output (#)	g_c (e^-/DN)	g_{pp} (eV/DN)
NRS1	17163	5.45	1	0.990	1.159
			2	0.989	1.158
			3	1.001	1.172
			4	1.005	1.176
			Mean	0.996	1.167
NRS2	17280	5.37	1	1.119	1.320
			2	1.123	1.325
			3	1.142	1.347
			4	1.165	1.375
			Mean	1.137	1.342

Table 1 evaluates Equation 3 for the two NIRSpec detectors. For more information about NIRSpec’s H2RG detectors, the reader is referred to [Rauscher et al. \(2014\)](#). For more information about H2RG detectors in general, we refer the interested reader to [Loose et al. \(2003, 2007\)](#).

2.3. *NIRSpec Radiation Shielding*

Radiation shielding is provided by the molybdenum (Mo) focal plane assembly (FPA) structure, the silicon carbide (SiC) camera housing, various SiC mirrors, and the SiC optical bench. Roughly speaking, there are about 20 mm of SiC shielding on the side of the detectors that light enters from. There are about 12 mm of Mo shielding on the back side. Shielding on the back side includes the Mo pedestal visible in Figure 3 and the Mo focal plane assembly itself.

The low energy electrons in the solar wind do not penetrate the science instruments, much less the engineered radiation shielding. The National Institute of Standards and Technology (NIST) Stopping Power and Range Tables for Protons (PSTAR)⁴ program calculates stopping power and range tables for protons in various materials. Using PSTAR, we calculate that this shielding blocks essentially all solar protons during solar-calm periods. It also blocks GCRs having energy $\lesssim 100$ MeV.

2.4. *Pre-Launch Expectations*

Several studies were done before launch to understand the cosmic ray environment at L2 and how NIRSpec’s

⁴ <https://physics.nist.gov/PhysRefData/Star/Text/PSTAR.html>

detectors might respond to it, including [Evans et al. \(2003\)](#) that describes the natural environment at L2, with a short discussion of radiation effects. [Barth et al. \(2000\)](#) focused specifically on the radiation environment and provided the pre-launch “nominal” cosmic ray rate estimate of $5 \text{ ions cm}^{-2} \text{ s}^{-1}$. [Pickel et al. \(2002\)](#) used physical modeling to study how semiconductor detector arrays respond to ionizing radiation. Pickel’s work was done before the flight detector designs were finalized. Although Pickel *et al.* included physical models of charge spreading, it could not simulate flight-like *JWST* detectors because the design parameters were not yet known.

As high energy ions traverse the HgCdTe detectors they leave trails of holes that are collected by the pixels. Here we deviate from the convention established in Section 2.2 because it is important to understand that holes are being collected. These holes integrate in the photodiodes and are then read out with other holes freed by photons from the telescope. Minimum ionizing protons (MIP), around 2 GeV, deposit about $1 \text{ keV}/\mu\text{m}$ as they travel through the detector. Since the rise of energy deposit is only logarithmic with the rise of the proton energy, this minimum is a reasonable approximation for typical cosmic rays. The detector thickness is $\sim 5 \mu\text{m}$ leading to a prediction of $\sim 5 \text{ keV}$ for protons normal to the detectors.

[Giardino et al. \(2019\)](#) examined how mitigating cosmic rays in the pipeline would affect NIRSpec sensitivity. They used a library of simulated cosmic ray hits to study the effect of the planned pipeline cosmic ray mitigation on NIRSpec noise. Giardino *et al.* injected theoretical cosmic rays into real NIRSpec ground test data. They predicted that overall effect of cosmic ray mitigation by the pipeline would increase NIRSpec’s noise by about 7%. [Birkmann et al. \(2022\)](#) studied NIRSpec’s total noise during commissioning and found that the measured values were consistent with pre-flight predictions.

3. DATA

3.1. *NIRSpec* Darks

The data come from three “Full Frame Dark Monitor” programs. The Program IDs are 1484, 4455, and 6633 in Cycles 1, 2, and 3 respectively. The files are available from the Mikulski Archive for Space Telescopes (MAST)⁵ at the Space Telescope Science Institute (STScI). We used all available IRS² darks from these programs through 13 February 2025. The integrations use NIRSpec’s NRSIRS2RAPID mode. This

resets the detector pixel-by-pixel, and then acquires 200 non-destructive samples up-the-ramp at a constant $t_f = 14.58889$ seconds per frame cadence. Nearly every pixel is disturbed by a cosmic ray during the roughly 49 minute integration time.

3.2. *Up-the-ramp* Readout

NIRSpec uses a sampling “up-the-ramp” readout scheme. Each 2048×2048 pixel detector is read out in four 512×2048 pixel stripes. Both detectors and all stripes are clocked synchronously. Within a stripe, there are 512 pixels in the fast-scan direction and 2048 lines in the slow-scan direction. The detectors are clocked at a constant t_f frame cadence. Destructive reset frames and non-destructive read frames have identical pixel timing.

In up-the-ramp sampling, each integration begins with a reset frame. Then, the system acquires the desired number of non-destructive reads. When there is light on the detector, a plot of the signal in a pixel versus time increases approximately linearly (“up-the-ramp”) until saturation is approached. More information about NIRSpec’s clocking patterns can be found in the online *JWST* User Documentation.⁶

3.3. *JWST* Pipeline Processing

We used Stage 1 of the *JWST* pipeline to process the uncalibrated data (filename suffix `_uncal.fits`).⁷ The pipeline is readily configurable giving users the option of choosing which steps to apply. We used the default settings in pipeline version 1.13.4 to apply `dq_init_step`, `saturation_step`, `superbias_step`, `refpix_step`, and `linearity_step` to all of the `_uncal.fits` files.

The first two steps are housekeeping. Then, `superbias_step` removes the approximately constant detector bias pattern. For NIRSpec, `refpix_step` applies the IRS² reference correction. Finally, `linearity_step` corrects for classical, signal-dependent nonlinearity. The resulting `_linearitystep.fits` files are the input to our own cosmic ray finder.

3.4. *Cosmic Ray Finder* Algorithm

To have as much control as possible, we wrote our own cosmic ray finder (*i.e.* we did not use the pipeline’s `jump_step`). First, data is processed to find the typical (RMS) noise and dark current in each pixel. A few ($< 3\%$) pixels are excluded from the study because their

⁶ <https://jwst-docs.stsci.edu/jwst-near-infrared-spectrograph/nirspec-instrumentation/nirspec-detectors/nirspec-detector-readout-modes-and-patterns>

⁷ https://jwst-docs.stsci.edu/jwst-science-calibration-pipeline/stages-of-jwst-data-processing/calwebb_detector1

⁵ <https://archive.stsci.edu/>

noise is too high or too low. To find cosmic ray hits in the dark data, each frame up-the-ramp is subtracted from the subsequent frame, resulting in 199 difference frames for each ramp. The difference frames are then scanned to find pixels with more than 7 times the RMS noise for this pixel. Since these are differences this is effectively a 5 sigma effect (randomly about once per difference-frame). Then neighboring pixels are added to the hit if they exceed 5 times the noise. The time, position, number of pixels, number of electrons and other information is recorded for each hit.

4. RESULTS

This section describes our characterization of cosmic ray interactions observed by NIRSpec. We begin with general considerations for hit detection, including effective detector area and energy thresholds (Section 4.1). We then analyze the particle hit rates (Section 4.2), the energy deposited by individual events (Section 4.3), their effect on noise (Section 4.4), their size measured in pixels on the detectors (Section 4.5), and finally the nature of the largest energy deposition events (Section 4.6).

4.1. General Considerations for Hit Detection

At the low end of the energy spectrum (< 1 keV), the imputed number of cosmic ray events is sensitive to the low energy cutoff, single-pixel event criteria, and how bad pixels are dealt with. For robustness, our reported hit characteristics and rates are therefore based on events depositing energies > 1 keV. This 1 keV threshold intentionally excludes a population of lower-energy interactions, leading to an undercount of the total GCR event rate. Based on statistical extrapolation from the events detected above 1 keV, we estimate that these uncounted low-energy hits constitute an additional 7 ± 2 % of the particle hits reported using the > 1 keV criterion.

Because of pixel operability differences between NIRSpec’s two detectors, the detectors have slightly different effective areas for integrating cosmic ray hits. The arrays have 2048×2048 square pixels, with each pixel being $18 \mu\text{m}$ on a side, resulting in a geometric area of 13.59 cm^2 per array. However, the outer 4 rows and columns are reference pixels, and some science pixels exhibit high noise or are otherwise poorly functioning. The net cosmic ray detection efficiency is 98% for NRS1 and 96.5% for NRS2.

After correcting for this detection efficiency, the hit rates measured on the two detectors match quite well, with any residual difference (a consistently $\sim 1.78\%$ higher rate for SCA NRS2) being within the uncertainties of conversion gain and other factors, and not statistically significant for this study. We therefore combine

data from the two detectors for all subsequently reported results.

4.2. Particle Hit Rate

One significant result is that NIRSpec’s measured cosmic ray hit rate at L2 is somewhat less than the pre-flight prediction of $5 \text{ ions cm}^{-2} \text{ s}^{-1}$ “nominal” (Barth et al. 2000). We discuss this further in Section 5, where we show that NIRSpec is likely to experience roughly $2.3 - 6 \text{ ions cm}^{-2} \text{ s}^{-1}$ depending on solar activity, with the mean being around $4.2 \text{ ions cm}^{-2} \text{ s}^{-1}$. The observed mean rate of $\sim 4.2 \text{ ions cm}^{-2} \text{ s}^{-1}$ represents an approximately 16% reduction from the pre-flight nominal prediction. While seemingly modest, this reduction translates directly into meaningful scientific benefits through its positive impact on noise.

4.3. Particle Hit Energy

The observed spectrum of particle hit energies is shown in Figure 4. There is a clear peak around 6 keV, with the spectrum falling off at both lower and higher energies. This peak is consistent with the ~ 5 keV energy deposition predicted for normally incident minimum ionizing particles (MIP), especially when considering a range of incidence angles. The shoulder observed around 70 keV in Figure 4 corresponds to the approximate full well capacity of the pixels ($\sim 60,000$ charges, or ~ 70 keV using the average pair-production gain from Table 1). This shoulder is likely an artifact of detector response, possibly due to reduced collection efficiency as pixels saturate, rather than a true feature of the incident cosmic ray spectrum. There are a few events depositing greater than 10 MeV total energy, but their numbers are low, and the corresponding statistics are poor. While rare, these very large events require special handling by the calibration pipeline.

To understand the expected energy deposition from MIPs, we used NIST’s PSTAR calculator⁸ to help determine elemental proton stopping powers. These are needed to calculate the energy deposition in $\text{Hg}_{0.7}\text{Cd}_{0.3}\text{Te}$ from 1–3 GeV protons. Unfortunately, the PSTAR webpage does not list Hg, Cd, or Te. We therefore interpolated between the listed materials, including adjustments based on atomic number to mass ratio trends. We inferred that the mass stopping powers for 1–3 GeV protons are approximately 1.16, 1.32, and $1.33 \text{ MeV cm}^2 \text{ g}^{-1}$ for Hg, Cd, and Te, respectively.

⁸ <https://physics.nist.gov/PhysRefData/Star/Text/PSTAR.html>

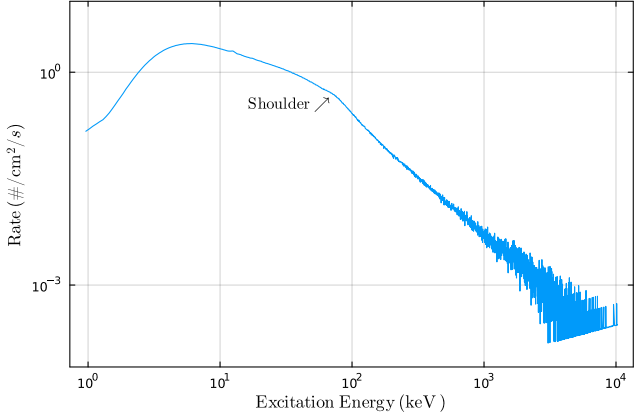


Figure 4. This histogram shows the distribution of energies of the impacts. There is a broad peak around 6 keV which is what is expected for minimum ionizing protons randomly impinging on the detector. The shoulder around 70 keV is likely due to the pixel wells filling which may affect the detector efficiency for higher energy particles. At the high end there are only a few particles in each bin which leads to the visible shot noise. The bin width is proportional to the square root of the energy, and then normalized so the rate is just the number per area and time.

Table 2. NIRSpec $\text{Hg}_{1-x}\text{Cd}_x\text{Te}$ Material Parameters

Element	x	Atom	Mass	Atomic	Atomic	σ_{pn}^a
		Fraction	Fraction	Number	Weight	(barn)
Hg	0.7	0.35	0.465	80	200.592	1.8117
Cd	0.3	0.15	0.112	48	112.414	1.2072
Te	1.0	0.5	0.423	52	127.6	1.3154

^a Cross section for 1 GeV inelastic proton-nucleus scattering.

We used the empirical Bragg Additivity Rule⁹ to compute the detector’s stopping power. It states that the stopping power of a compound is equal to the sum of the stopping powers of its constituent elements weighted by their mass fractions. Table 2 shows the mass fractions for NIRSpec’s detectors. Applying Bragg’s rule to NIRSpec’s detectors yields a combined mass stopping power of $1.25 \text{ MeV cm}^2 \text{ g}^{-1}$. This value corresponds to an energy loss of about 5 keV for normal incidence, minimum ionizing protons traversing a $5 \mu\text{m}$ thick detector layer, assuming a material density of approximately 7.87 g cm^{-3} .

⁹ As described in, *e.g.*, International Commission on Radiation Units and Measurements (ICRU) (1993)

4.4. Effect on Noise

Although Stage 1 of the *JWST* pipeline finds and corrects for cosmic rays, doing so comes at a price: increased noise. This happens in two main ways. First, the pipeline can miss smaller cosmic ray hits, leaving them in the data. Second, for the cosmic rays it does find, the pipeline tries to salvage all the good data. Instead of discarding the ramp after a hit, it calculates the slope of the ramp before and after the hit when possible. It then computes a weighted average of these two slopes to get the final count rate. The trade-off is that each of those shorter segments gives a less certain—and therefore noisier—slope measurement. Averaging them results in a final rate that is still noisier than what one would get from a single, uninterrupted integration.

Before launch, Giardino et al. (2019) used Monte Carlo simulation to predict that cosmic rays would degrade NIRSpec’s total noise by about 7% compared to the on-ground performance. Birkmann et al. (2022) subsequently reported that this prediction had borne out after launch. Knowing the average number of pixels disturbed by cosmic rays is therefore an important parameter for Exposure Time Calculators (ETC).

4.5. Particle Hit Area

Figure 5 shows the measured cosmic ray hit area histogram. The mean hit area is about 7.1 pixels. This observed mean is smaller than the typical hit size of up to 9 pixels assumed in pre-flight *JWST* ETC planning.

We were initially surprised by the local minimum at 5 pixels. It is a robust feature that appears in both NIRSpec detectors, in multiple cuts through the data, and in other *JWST* instruments (Martel et al. 2024). Intuitively, we had expected the peak to be at 5 pixels because a perfectly centered hit at normal incidence would clearly disturb the hit pixel. We furthermore expected inter-pixel capacitance (IPC; Moore 2006) to couple it to the four nearest neighbors yielding an initial estimate of 5 pixels.

To further explore this, we constructed simple Monte Carlo models. We found that the shape of the energy spectrum (Figure 4) produces a local minimum at 5 pixels, and that we could change the detailed shape of the histogram by varying the hit detection thresholds. We therefore believe that the local minimum at 5 pixels is caused by the shape of the cosmic ray energy spectrum and tunable by adjusting detection thresholds.

4.6. The Largest Cosmic Ray Events

The largest observed cosmic ray events often manifest as “snowballs”; or more rarely, they appear as extremely

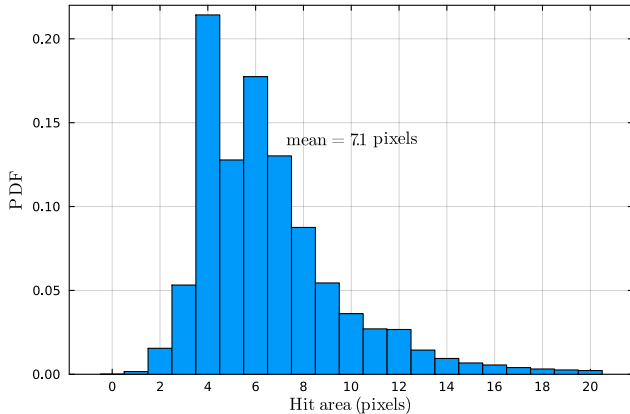


Figure 5. This histogram shows the probability density function of cosmic ray hit sizes. It combines data from the two NIRSpec detectors. The mean hit area is 7.1 pixels. The local minimum at 5 pixels is a robust feature, appearing in both detectors and in different subsets of data. Similar minima can be reproduced in Monte Carlo simulations using the measured hit rate versus energy spectrum (see Figure 4) as input. In these simulations, the precise characteristics of the local minimum (such as its depth, exact position, or number of local minima) were found to be sensitive to the selection thresholds applied. In general, hit area correlates with energy deposition. We have cropped off some very energetic hits to show the main histogram better.

intense events with associated showers.¹⁰ The term snowball was coined circa 2005 to describe very large, circular, saturating, cosmic-ray-like signatures identified during ground testing of *JWST* and *HST* WFC3 detectors.

On orbit, NIRSpec sees something similar to the historical snowballs, as well as more exotic events including some with showers of secondary particles. The showers that we see in NIRSpec data are different from the shower phenomenon that has been described in the *JWST* MIRI.^{4,6}

The definitive root cause of snowballs observed in ground tests was not established before *JWST*'s launch, though alpha-emitting radioactive contaminants on or near the detectors were considered a possible source. On orbit, the large energy depositions, which manifest as both compact snowballs and, more rarely, as energetic events with associated secondary showers, are thought to originate from several mechanisms.

One candidate is the direct impact of highly ionizing GCRs, such as heavy ions; an iron nucleus, for example, deposits substantially more energy ($Z^2 \approx 676$ times greater for charge $Z = 26$) than a proton of the same

velocity and can readily cause extensive pixel saturation. Alternatively, these large events might result from secondary particles produced when primary GCRs interact within the observatory's shielding or the detector material itself. Among such secondaries, those with low energy (e.g., alpha particles or nuclear spallation fragments) that stop within the thin detector layer could explain snowballs that appear almost perfectly circular. In contrast, events that are elongated and feature collimated showers of particles may be more consistent with complex interactions involving surrounding material and the detector material, or occasionally, high-energy inelastic scattering of GCRs occurring directly within the detector material.

Figure 6 presents six examples of very large cosmic ray hits observed on the NIRSpec detectors. Panel (a) of Figure 6 displays a roughly circular, strongly saturated hit, often referred to as a snowball. Panels (b) and (c) exhibit more complex structures identified as secondary showers. These features are consistent with high-energy GCRs undergoing complex interactions with the detector and surrounding material or perhaps nuclear interactions within the HgCdTe detector material, leading to an often collimated cascade of secondary particles. A different type of nuclear interaction is depicted in panel (d), characterized by a significant deviation in the primary particle's path or the creation of a short, highly ionizing recoil track. Panel (e) illustrates a curved track, which suggests the passage of a very low-energy particle; such a trajectory could be produced by, for instance, a secondary alpha particle originating from radioactive decay within the instrument shielding or nearby materials. Finally, panel (f) shows a broken or discontinuous track. This morphology might be attributed to a particle traversing both the HgCdTe detector layer and the underlying Readout Integrated Circuit (ROIC). These two components are separated by a gap of approximately a few microns, and a particle crossing this void would not deposit charge, leading to the observed break in the track.

Snowballs have a typical structure (Figure 7). At the center is a heavily saturated core, where the charge deposited by the particle exceeds the full well capacity of the pixels. Surrounding this core is a “shoulder” region, where the collected charge diminishes rapidly with increasing radial distance from the impact center. Beyond this shoulder extends a faint, diffuse halo. A key characteristic of this extended halo is that its surface brightness profile typically follows an $\sim r^{-3}$ power law, where r is the radial distance from the event's core. We do not have a satisfactory explanation for this empirical relation at this time.

¹⁰ <https://jwst-docs.stsci.edu/known-issues-with-jwst-data/shower-and-snowball-artifacts/#ShowerandSnowballArtifacts-Snowballssnowballs>

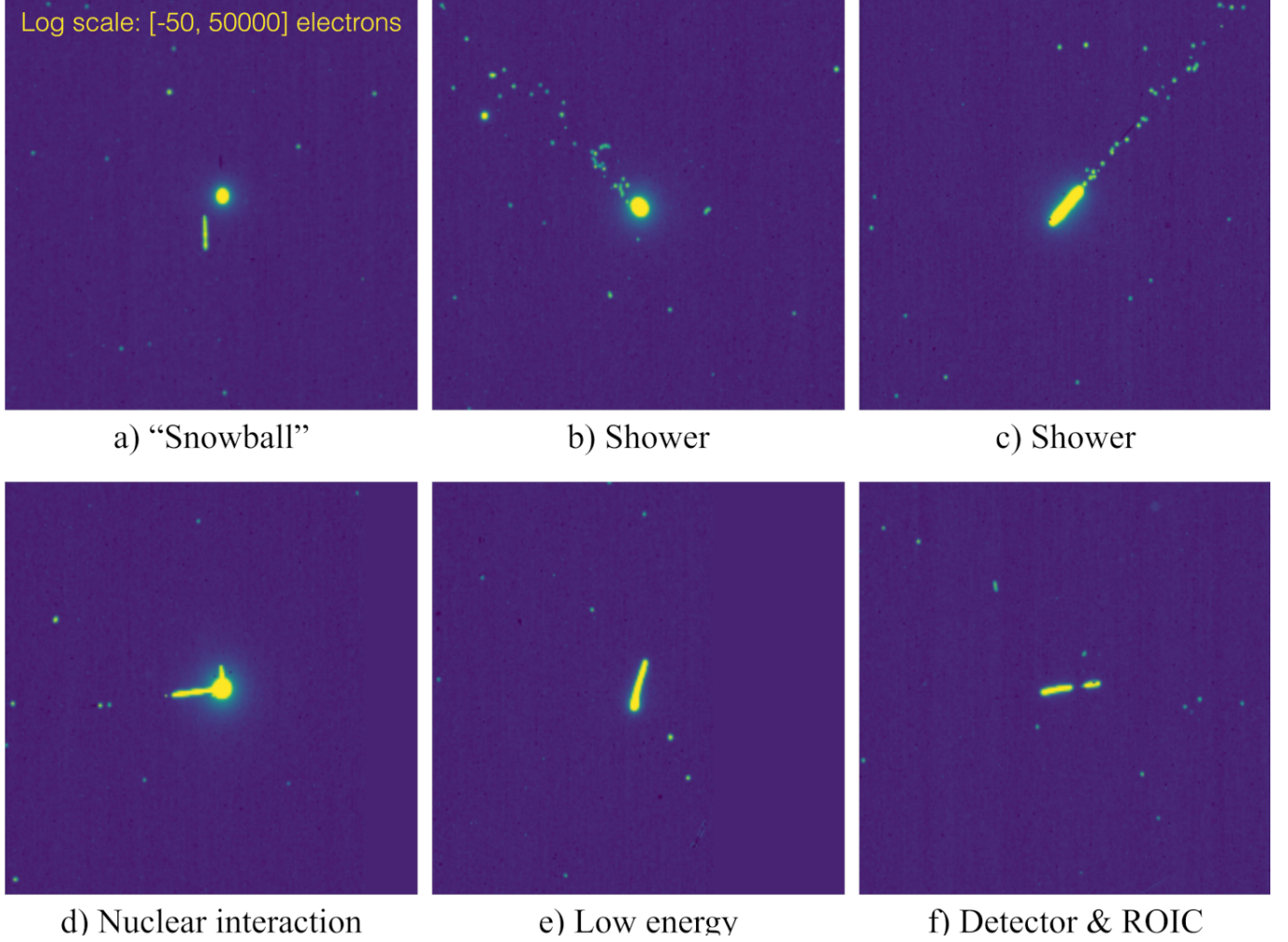


Figure 6. Examples of large cosmic ray hit morphologies. (a) Snowballs are round, with saturated cores, and usually no showers. (b-c) Secondary showers. (d) Possible inelastic scattering. (e) Curved track potentially from low-energy particle. (f) Broken track possibly due to particle traversal of both detector material and ROIC.

Some of the hits like those shown in Figure 6(b-d) suggest inelastic scattering in the HgCdTe detector material. To test this hypothesis, we computed the probability that a 1 GeV proton might undergo inelastic scattering while passing through the $\sim 5 \mu\text{m}$ thick detector layer at 45° incidence.

Letaw et al. (1983) provides an empirical formula for the proton-nucleus inelastic scattering cross sections of Hg, Cd, and Te that is accurate to a few percent at 1 GeV,

$$\sigma(E) = 45A^{0.7} [1 + 0.016 \sin(5.3 - 2.63 \ln A)] \times [1 - 0.62e^{-E/200} \sin(10.9E^{-0.28})] \text{ mb.} \quad (4)$$

In this expression, A is atomic mass and E is proton energy in MeV. Table 2 evaluates this expression for NIRSpec's detectors. To compute the total inelastic scattering cross section per unit volume, one sums the cross

sections of the constituent atoms. This is straightforwardly done using the density and mass fractions of the elements from Table 2.

Assuming the same $\rho = 7.87 \text{ g cm}^{-3}$ density as before, the inelastic scattering cross section per unit volume for 1 GeV protons in NIRSpec's detectors is $\mu = 4.63 \times 10^{-6} \mu\text{m}^{-1}$. The probability of any one proton, incident at 45° , undergoing inelastic scattering is,

$$p = 1 - e^{-\mu\sqrt{2}\ell}, \quad (5)$$

where ℓ is the HgCdTe detector layer's thickness. With $\ell = 5 \mu\text{m}$, the result is $p = 3.27 \times 10^{-5}$.

The average GCR rate since launch has been about $3.3 \text{ ions cm}^{-2} \text{ s}^{-1}$. Integrating over the entire data set and assuming that 90% of the events are protons, about 3.6×10^7 protons struck NIRSpec's detectors, and of these we would expect a little over 1,000 to have undergone inelastic scattering. While we have not tried to

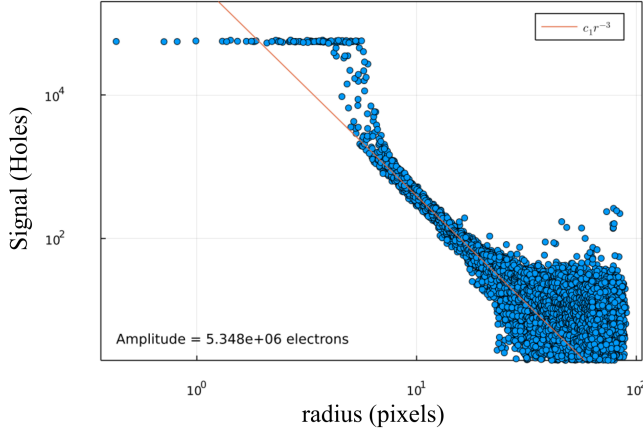


Figure 7. Radial profile of a typical large snowball halo cosmic ray event. The plot shows the saturated core, the shoulder region with a steep decline in charge, and the extended halo exhibiting an r^{-3} falloff (indicated by the fitted line). The x-axis represents radial distance from the core, and the y-axis represents signal intensity or charge.

carefully count showers and other evidence of potential inelastic scattering, this is broadly consistent with the observation that showers are a very rare yet nevertheless real feature in the data. Based on this, inelastic scattering in the HgCdTe seems a plausible explanation for at least some events like those in Figure 6(b-d).

Although events with large haloes constitute only a small fraction of GCRs, they are nevertheless important to the pipeline. Snowballs were first identified because of their round, completely saturated cores. Arbitrarily setting 9 pixels as the lower limit on core size, an event must dissipate $\gtrsim 1$ MeV in the detector to potentially create a snowball. In these data, the corresponding snowball rate is about 0.3 snowballs per 14.58889 second NIRSpec frame, or 0.0015 snowballs $\text{cm}^{-2} \text{s}^{-1}$. This is very roughly $> 100\times$ higher than was observed during *JWST* ground integration and testing.¹¹ Any full-frame NIRSpec integration longer than about a minute will probably have some snowballs in it. The pipeline therefore needs to be aware that pixels potentially far from a snowball might be disturbed and treat them accordingly.

Providing detailed explanations for the complex, high energy events is beyond the scope of this paper. In September, 2023, the authors gave a seminar at Fermilab. Many attendees were particle physicists. Their consensus view was that the high energy events could probably be explained using Geant4 (GEometry AND

¹¹ Although we see snowballs both on the ground at L2, the vastly different rates indicate different causative mechanisms.

Tracking 4)¹². We would be happy to share our catalog of NIRSpec cosmic ray hits upon request.

5. COMPARISON TO OTHER MISSIONS

Figure 8 shows the measured *JWST* NIRSpec hit rates overlaid on hit rates from two relevant space missions, ACE and GOES. This section provides more background on *ACE* and *GOES*. Then, building on all available data, we discuss what *JWST* and *Roman* should see in the next few years.

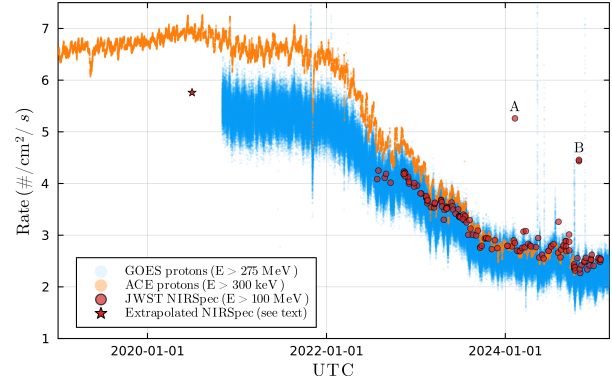


Figure 8. This figure shows the cosmic ion fluxes seen by NIRSpec's two detectors overlaid on some cosmic proton fluxes seen by relevant missions. *ACE* is located in deep space at L1. The *ACE* plot is fairly smooth because the downloadable data exclude periods of high solar activity. For comparison, we show *GOES-16*. As described in the text, we have integrated the *GOES* proton data over energies $E > 100$ MeV to mimic the effects of NIRSpec's shielding. The *GOES* flux is lower because the Earth's magnetosphere provides additional shielding of GCRs in *GOES*' geostationary orbit that *JWST* does not experience at L2. NIRSpec happened to be acquiring calibration darks during two periods of enhanced solar activity. These are labeled A and B. This shows that some solar particles are able to get through during periods of enhanced solar activity, although the effect would not have stopped science observations during these periods. *JWST* launched near solar minimum, and it has seen nearly the full solar cycle. During this period, cosmic ray fluxes ranged from about $4.3 - 2.3$ ions $\text{cm}^{-2} \text{s}^{-1}$ excluding points A and B. During the previous solar cycle, Kirsch (2018) measured a range of $2 - 4$ ions $\text{cm}^{-2} \text{s}^{-1}$ using Gaia.

5.1. ACE

NASA's *ACE* was launched into a Sun/Earth-Moon L1 Lissajous orbit in August, 1997 (Stone et al. 1998). This orbit was chosen to provide continuous monitoring of the solar wind, interplanetary magnetic field, and

¹² <https://geant4.web.cern.ch/>

energetic particle populations before they interact with the Earth’s magnetosphere. ACE’s primary scientific objective is to determine and compare the elemental and isotopic composition of matter from diverse sources, including the solar corona (via solar wind and solar energetic particles, SEPs), the interplanetary medium, the local interstellar medium, and GCRs (Chiu et al. 1998). During quiescent periods, it is mostly high energy GCRs that have sufficient energy to penetrate NIRSpec’s radiation shielding.

ACE characterizes the space radiation environment using a suite of nine instruments (Stone et al. 1998). Of these, the Cosmic Ray Isotope Spectrometer (CRIS) is particularly important for characterizing GCRs relevant to this study. CRIS is designed to measure the elemental and isotopic composition of GCR nuclei from Helium, $Z = 2$ to Zinc $Z = 30$ “and beyond”,¹³ using four identical stacks of large-area silicon solid-state detectors. Each stack includes detectors designated E1 through E8 for energy deposition measurements. An additional detector, E9, located at the bottom of each stack, is used in anticoincidence to identify and guard against particles that penetrate the entire detector stack. The “singles rate” from this E9 detector provides a measure of the flux of these highly penetrating particles.

Although the overall radiation environment at L1 differs from that at L2, the most important differences have to do with plasmas that are mostly blocked by *JWST* structure and the NIRSpec detectors’ radiation shielding. Since both L1 and L2 are well outside Earth’s magnetosphere, we expect the GCR environments to be similar for ACE and *JWST*.

For Figure 8, we downloaded contributed “Level 3” data from the Ace Science Center.¹⁴ According to the website, these are the hourly averaged CRIS E9 rate, after cuts to clean the data of artifacts and remove active periods (SEPs). According to a note provided with the data, during solar quiet periods the singles count rate is probably dominated by GCR protons at energies > 120 MeV. The note cautions that the singles data are not carefully calibrated. But, because of the detector’s large area (4 10-cm diameter 3-mm thick Si detectors) the statistical accuracy of its count rate is quite high. For our purposes, we treat the ACE data as one of several points of comparison for the NIRSpec data that are our main focus.

5.2. GOES-16

GOES-16 (hereafter “*GOES*”) directly measures proton fluxes in the outer regions of the Earth’s magnetosphere. Although *GOES*’s GEO orbit is inside the Earth’s magnetosphere, the magnetic field is quite weak at $r_{\text{GEO}} = 6.6 r_{\oplus}$. One would therefore expect the Earth’s magnetosphere to provide only weak shielding of cosmic rays sufficiently energetic to penetrate NIRSpec’s shielding in GEO.

The most relevant instrument for our purposes is the Space Environment In-Situ Suite (SEISS) Solar and Galactic Proton Sensor (SGPS). It covers a broad energy range from 1 MeV to >500 MeV. The SGPS differential channels were designed and calibrated to measure Solar Particle Events (SPE). These are characterized by high particle flux that falls off rapidly with increasing particle energy. Most SPE particles are blocked in NIRSpec’s shielding. However, high energy GCRs pass completely through. Fortunately, SGPS channels P10 (275–500 MeV) and P11 (> 500 MeV) are calibrated for use during solar quiet conditions.

5.3. Predictions for JWST

The Sun modulates GCRs in the solar system. The GCR rate is low when the Sun is active and vice versa. The mechanism is thought to be the stronger, tangled magnetic fields that appear in the heliosphere when the sun is particularly active. These act to deflect charge particles away from the inner solar system.

Figure 9 plots the number of sunspots versus date during the current and last solar cycle. It shows that at the time of *JWST*’s launch in December, 2021, solar activity was near its minimum. The first 6 months of *JWST*’s mission were spent commissioning the observatory. *JWST* started collecting science data, and taking regular calibrations, in June, 2022. This is indicated by region B in the plot.

Looking forward, we expect *JWST* to experience the declining phase of Solar Cycle 25. As solar activity falls, the cosmic ray rate will increase from about $2.3 - 4.3 \text{ ions cm}^{-2} \text{ s}^{-1}$ between now and mid-2027. It will then continue to increase, peaking perhaps around $6 \text{ ions cm}^{-2} \text{ s}^{-1}$ in the early 2030s. The cycle will then repeat itself scaled by the strength of the next Solar Cycle.

We see no reason why the characteristics of individual hits would change significantly. We therefore expect the typical hit to disturb about 7.1 pixels sufficiently to require mitigation.

6. EXPECTATIONS FOR ROMAN SPACE TELESCOPE

Roman, scheduled for launch no later than May, 2027, is NASA’s next astrophysics flagship mission. Similar

¹³ https://izw1.caltech.edu/ACE/CRIS_SIS/cris.html#gcr

¹⁴ <https://izw1.caltech.edu/ACE/ASC/DATA/level3/cris/GCRprotons/CRIShourlyE9rates.txt>

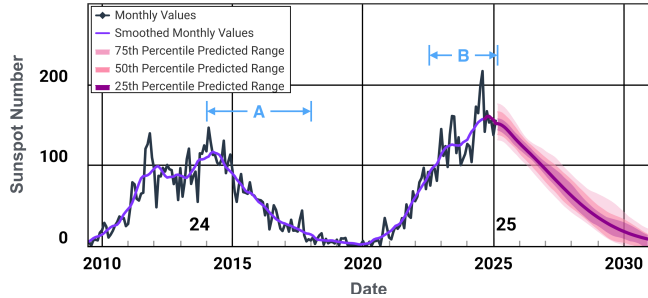


Figure 9. Sunspot number is correlated with solar activity and inversely correlated with the GCR rate. This plot shows sunspot number during: (A) a period when the Gaia CCDs saw between $2 - 4$ protons $\text{cm}^{-2} \text{ s}^{-1}$ (Kirsch 2018) and (B) this study. Like *JWST*, Gaia is in an L2 orbit. Credit: National Solar Observatory, <https://www.swpc.noaa.gov/products/solar-cycle-progression>

to *JWST*, *Roman* will operate from a L2 quasi-halo orbit. This will expose it to a GCR environment similar to *JWST*'s. *Roman*'s launch is anticipated during the declining phase of Solar Cycle 25, roughly midway between its recent maximum and the next minimum (see Figure 9).

For its Wide Field Imager (WFI), *Roman* will use Teledyne H4RG-10 HgCdTe detectors with a shorter cutoff wavelength ($\lambda_{\text{co}} = 2.5 \mu\text{m}$) than NIRSpec's. Mosby et al. (2020) describes these detectors in detail. Key detector differences from NIRSpec will influence cosmic ray manifestations:

1. **Smaller Pixels:** $10 \mu\text{m}$ pitch versus NIRSpec's $18 \mu\text{m}$.
2. **Thinner Active Layer:** The HgCdTe layer is likely a little thinner.
3. **Reduced Charge Diffusion:** Lateral charge spread is anticipated to be less on account of the somewhat thinner active layer and higher photodiode reverse bias.

The WFI's radiation shielding's effectiveness is probably similar to NIRSpec's. The H4RG-10's molybdenum package is broadly similar to the NIRSpec H2RG package vis-à-vis shielding.

The detector differences will affect how hits manifest. While a thinner layer and less diffusion might imply smaller charge clouds, the significantly smaller pixels might cause an event to disturb more pixels. A typical *Roman* hit might affect somewhat more pixels than NIRSpec's ~ 7.1 , though the increase should not be drastic.

Roman's $\lambda_{\text{co}} = 2.5 \mu\text{m}$ cutoff implies that its HgCdTe has a bandgap roughly twice as wide as that of NIRSpec's $\lambda_{\text{co}} = 5.3 \mu\text{m}$ material. This wider bandgap will

halve the number of electron-hole pairs generated per keV of deposited energy. A typical *Roman* GCR event will likely produce only about half the charge in the detector layer as a similar NIRSpec event.

Regarding GCR interaction rates, assuming solar activity (the remainder of Solar Cycle 25 and the onset of Solar Cycle 26) follows typical modulation patterns, *Roman* will likely launch into a GCR flux of approximately $4.3 \text{ ions cm}^{-2} \text{ s}^{-1}$. Towards the Solar Cycle 25 minimum (expected in the early 2030s), this rate could increase to $\sim 6 \text{ ions cm}^{-2} \text{ s}^{-1}$. Subsequently, as Solar Cycle 26 activity rises, the GCR flux should decrease, possibly returning to $4.3 \text{ ions cm}^{-2} \text{ s}^{-1}$ roughly five years post-launch (circa early 2032).

7. SUMMARY

We describe cosmic ray impacts on *JWST* NIRSpec's $\lambda_{\text{co}} = 5.4 \mu\text{m}$ cutoff HgCdTe H2RG detectors using dark exposures from NIRSpec's first three years of operations at L2. These detectors do not directly see the L2 radiation environment. Rather, they sit behind shielding that was designed to meet a requirement of greater than 10 mm aluminum-equivalent over 4π steradians. The shielding effectively blocks solar particles except during periods of high solar activity. High energy GCRs ($E > 100 \text{ keV}$) penetrate the shielding and dominate the observed events. Our findings potentially inform ongoing *JWST* operations and future missions at L2 and in deep space having comparable shielding.

The NIRSpec GCR hit rate decreased from about 4.3 to $2.3 \text{ ions cm}^{-2} \text{ s}^{-1}$ during the period June, 2022, to February, 2025. This was driven by increasing solar activity on the rising side of Solar Cycle 25. A typical GCR hit affects ~ 7.1 pixels and deposits $\sim 6 \text{ keV}$ (equivalent to ~ 5200 charges) in the detector material. This corresponds to a linear energy transfer of $\sim 0.86 \text{ keV } \mu\text{m}^{-1}$. These characteristics overwhelm the read noise and highlight the need for robust cosmic ray mitigation, as is done in Stage 1 of the *JWST* pipeline.

Our investigation explored a surprisingly high number of large snowball events that were seen on-orbit (Section 4.6). Although snowballs were seen during ground testing, we see very roughly $100\times$ more of them on-orbit. Some of the largest events have associated secondary showers.

Very large cosmic ray hits may originate from several sources: direct impacts from heavy ions, secondary particles produced within NIRSpec's shielding, or complex interactions within or near the detector material, such as inelastic scattering within the HgCdTe, that produce particle showers.

Looking ahead for *JWST*, we expect the GCR hit rate to rise as solar activity declines. The rate should increase from its current $\sim 2.3 \text{ ions cm}^{-2} \text{ s}^{-1}$ to $\sim 4.3 \text{ ions cm}^{-2} \text{ s}^{-1}$ by early 2027, potentially reaching $\sim 6 \text{ ions cm}^{-2} \text{ s}^{-1}$ near the Solar Cycle 25 minimum in the early 2030s. Because the snowball rate tracks the GCR rate, we expect to see snowballs following the same trend.

These results should apply to *Roman* (Section 6). Planned for launch no later than May, 2027, *Roman* will enter its L2 orbit as Solar Cycle 25 wanes. *Roman* will likely experience an initial GCR flux near $4.3 \text{ ions cm}^{-2} \text{ s}^{-1}$. This rate is projected to rise to $\sim 6 \text{ ions cm}^{-2} \text{ s}^{-1}$ during solar minimum before declining back to $\sim 4.3 \text{ ions cm}^{-2} \text{ s}^{-1}$ near *Roman*'s fifth year at L2.

While *Roman*'s radiation shielding effectiveness should be comparable to NIRSpec's, its H4RG-10 HgCdTe detectors ($\lambda_{\text{co}} \approx 2.5 \mu\text{m}$) differ significantly. H4RG-10 detectors feature smaller pixels ($10 \mu\text{m}$ versus $18 \mu\text{m}$), perhaps a somewhat thinner absorber layer, and reduced charge diffusion on account of the thinner active layer. Though *Roman*'s hits may affect a somewhat larger number of its smaller pixels, we do not expect a dramatic difference. However, *Roman*'s wider detector bandgap will halve the electron-hole pairs generated per keV dissipated. A *Roman* GCR hit will produce only about half the charge seen in a NIRSpec event.

In summary, we find that cosmic rays at L2 are somewhat less disruptive for *JWST* NIRSpec than pre-

launch expectations. Before launch, *JWST* planned for 5 ions $\text{cm}^{-2} \text{ s}^{-1}$ "nominal", and for each event to disturb potentially as many as nine pixels. In practice, NIRSpec's average observed flux, if extrapolated over a full solar cycle, is about 16% lower than the pre-launch "nominal" expectation and typical events are about 20% smaller in pixels. Although very large snowball events, and events with showers are comparatively rare, they are nevertheless present in most full frame exposures. The largest events present unique challenges to calibration pipelines and would benefit from further study, perhaps using Geant4 to more fully understand the physical mechanisms.

¹ This work was supported by NASA as part of the
² James Webb and Nancy Grace Roman Space Telescope
³ Projects. Resources supporting this work were pro-
⁴ vided by the NASA High-End Computing (HEC) Pro-
⁵ gram through the NASA Center for Climate Simulation
⁶ (NCCS) at Goddard Space Flight Center. We thank
⁷ Maurice te Plate for helpful discussions about NIR-
⁸ Spec's radiation shielding. We acknowledge the use of
⁹ Google Gemini for assistance with spelling/typo cor-
¹⁰ rection, grammar, and stylistic improvements to this
¹¹ manuscript.

Facilities: *JWST* NIRSpec

Software: Julia (Bezanson et al. 2017)

REFERENCES

Alig, R. C., & Bloom, S. 1977, Phys. Rev. Lett., 35, 677

Barth, J. L., Isaacs, J. C., & Poivey, C. 2000, Next Generation Space Telescope Program

Bezanson, J., Edelman, A., Karpinski, S., & Shah, V. B. 2017, SIAM Rev., 59, 65, doi: [10.1137/141000671](https://doi.org/10.1137/141000671)

Birkmann, S. M., Giardino, G., Sirianni, M., et al. 2022, Proc SPIE, 12180, 101

Chiu, M. C., Haggerty, D. K., Bustard, W. C., et al. 1998, Space Science Reviews, 86, 257, doi: [10.1023/A:100501022ACE](https://doi.org/10.1023/A:100501022ACE)

Evans, S. W., et al. 2003, Next Generation Space Telescope Program

Fox, O., Waczynski, A., Wen, Y., et al. 2009, PASP, 121, 743, doi: [10.1086/605131](https://doi.org/10.1086/605131)

Gardner, J. P., Mather, J. C., Abbott, R., et al. 2023, PASP, 135, 68001, doi: [10.1088/1538-3873/acd1b5](https://doi.org/10.1088/1538-3873/acd1b5)

Giardino, G., Birkmann, S., Robberto, M., et al. 2019, PASP, 131, 94503, doi: [10.1088/1538-3873/ab2fd6](https://doi.org/10.1088/1538-3873/ab2fd6)

International Commission on Radiation Units and Measurements (ICRU). 1993, Stopping Powers and Ranges for Protons and Alpha Particles, ICRU Report No. 49 (Bethesda, MD: International Commission on Radiation Units and Measurements)

Jakobsen, P., Ferruit, P., Alves de Oliveira, C., et al. 2022, A&A, 661, A80, doi: [10.1051/0004-6361/202142663](https://doi.org/10.1051/0004-6361/202142663)

Kirsch, C. T. 2018, Master's Thesis Physics, Dr. Karl Remeis-Sternwarte Astron. Inst.

Letaw, J., Silberberg, R., & Tsao, C. 1983, ApJ Supp., 51, 271, doi: [10.1086/190849](https://doi.org/10.1086/190849)

Loose, M., Beletic, J., Garnett, J., & Xu, M. 2007, in Society of Photo-Optical Instrumentation Engineers (SPIE) Conference Series, Vol. 6690, Proc SPIE, ed. T. J. Grycewicz, C. J. Marshall, & P. G. Warren, 66900C, doi: [10.1117/12.735625](https://doi.org/10.1117/12.735625)

Loose, M., Farris, M. C., Garnett, J. D., Hall, D. N. B., & Kozlowski, L. J. 2003, Proc SPIE, 4850, 867

Martel, A., Cooper, R., & Volk, K. 2024, JWST Tech. Rep., JWST-STScI-008875

Moore, A. C. 2006, Opt. Eng., 45, 076402, doi: [10.1117/1.2219103](https://doi.org/10.1117/1.2219103)

Mosby, G., Rauscher, B. J., Bennett, C., et al. 2020, JATIS, 6, 46001, doi: [10.1117/1.JATIS.6.4.046001](https://doi.org/10.1117/1.JATIS.6.4.046001)

Pickel, J. C., Reed, R. A., Ladbury, R., et al. 2002, IEEE Trans. Nucl. Sci., 49 I, 2822, doi: [10.1109/TNS.2002.805382](https://doi.org/10.1109/TNS.2002.805382)

Rauscher, B. J., Boehm, N., Cagiano, S., et al. 2014, PASP, 000, doi: [10.1086/677681](https://doi.org/10.1086/677681)

Rauscher, B. J., Arendt, R. G., Fixsen, D. J., et al. 2017, PASP, 129, 105003, doi: [10.1088/1538-3873/aa83fd](https://doi.org/10.1088/1538-3873/aa83fd)

Stone, E. C., Frandsen, A. M., Mewaldt, R. A., et al. 1998, Space Science Reviews, 86, 1, doi: [10.1023/A:1005082526237](https://doi.org/10.1023/A:1005082526237)